Physics of Fluids

Advanced ultrasound techniques for studying liquid–liquid dispersions in confined impinging jets ⓔⓟ

Special Collection: Overview of Fundamental and Applied Research in Fluid Dynamics in UK

Fria Hossein; Cong Duan; Panagiota Angeli ✉ ⓘⓓ

Check for updates

View Online

Export Citation

30 August 2024 09:01:07

Physics of Fluids

Special Topic:

Fluid-Structure Interaction

Guest Editors: A-Man Zhang, Tiegang Liu, Boo Cheong Khoo and Nhan Phan-Thien

Submit Today!

AIP Publishing

AIP Publishing

Advanced ultrasound techniques for studying liquid–liquid dispersions in confined impinging jets ⓔⓟ

View Online   Export Citation   CrossMark

Fria Hossein, Cong Duan, and Panagiota Angeli[a)]ⓘⒹ

AFFILIATIONS

ThAMeS, Department of Chemical Engineering, University College London, Torrington Place, London WC1E 7JE, United Kingdom

Note: This paper is part of the special topic, Overview of Fundamental and Applied Research in Fluid Dynamics in UK.
[a)]Author to whom correspondence should be addressed: p.angeli@ucl.ac.uk

ABSTRACT

Advanced ultrasound techniques were used to study liquid–liquid dispersed flows formed in impinging jets confined in small channels. Ultrasound speed and attenuation coefficient spectra of the propagated sound waves were used to obtain volume fraction and drop size distributions, respectively. The results were compared against drop size distributions obtained with high-speed imaging. Experiments were conducted in a 2 mm internal diameter tube for both kerosene oil continuous and glycerol/water continuous dispersions. The overall mixture flow rate was set at 60 ml/s, and the dispersed phase fractions were 0.02, 0.05, and 0.10. The measured volume fractions were found to be very close to the input ones, indicating a very small slip between the phases in the dispersed flows. From the ultrasound measurements, the drop size distributions were found to range from 32 to 695 μm under the different conditions used. The drop sizes at the two low input volume fractions were in reasonable agreement with the results from the imaging. Imaging, however, could not be used for the 0.10 input dispersed phase fraction. These results demonstrate the applicability of the ultrasound techniques to measurements in dispersed liquid–liquid flows in small channels.

I. INTRODUCTION

In impinging jets, two liquid streams collide at high velocities. Depending on whether the liquids are miscible or immiscible, impinging jets result in efficient mixing or the generation of dispersions and find applications in intensified reactions and processing of food, pharmaceuticals, and cosmetics.[1,2]

Recently, impinging jets have been used to generate dispersions within the confinement of small channels (confined impinging jets, CIJ) in applications such as intensified solvent extraction and biofuel production.[3] In these configurations, the flow patterns and drop size depend on various factors such as fluid flow rates, fluid properties, jets diameter, and impingement angle.[4] For instance, higher impingement velocities can lead to the breakup of larger drops into smaller ones, thereby reducing the average drop size in the system.[5] The liquid properties are also important, and liquids with high viscosity or surface tension may form larger drops that persist longer in the flow.[6] The drop size distribution has significant effects on mass and heat transfer rates in multiphase processes.[7,8] Therefore, it is paramount to measure the

drop size distribution and drop volume fractions in such systems using techniques that allow fast, cost-effective, and reliable measurements.[9,10] Drop size and drop volume fraction are important for process efficiency and optimization, performance evaluation, and product quality assurance.[11] Current approaches for studying liquid–liquid dispersed flows involve sensors based on conductivity,[12] capacitance,[13] or local heat transfer,[14] which can be intrusive and potentially disruptive to the flow field. Imaging methods have advanced alongside improvements in digital and fast cameras, image processing capacity, and in high-energy, high-frequency lasers. Optical techniques such as high-speed imaging[15] and laser-based approaches, including planar laser induced fluorescence (PLIF)[16] and particle image velocimetry (PIV),[17] have also been utilized for measurements in liquid–liquid dispersed flows to investigate volume fractions, size distributions, and velocities of the dispersed phase. These optical methods are restricted to transparent test sections and fluids. Liquids with a matching refractive index can be used to increase the volume fractions that can be studied, but this restricts the range of suitable test liquids.[18] Furthermore, common

drawbacks in the application of electrical sensors include spatial resolution and the calibration procedure.[19] Additionally, techniques based on magnetic resonance or x-ray imaging can be used in opaque systems but are based on radiation and have cost and safety limitations; they rely on density differences between the phases, which limit the fluid ranges that can be studied.[20,21] Tomographic techniques that have been used in liquid–liquid systems include electrical capacitance tomography (ECT) as demonstrated by Hasan and Azzopardi,[22] and electromagnetic tomography (EMT) as shown by Wei and Soleimani.[23] While these techniques offer good accuracy, they are often associated with reduced spatial resolution and involve complex data processing methodologies.

Given these challenges, ultrasound techniques have risen as potential alternatives for measurements in liquid–liquid systems,[24] which can deliver rapid, cost-effective measurements that can be used in non-transparent systems and without harmful radiation. Moreover, they are suitable for use in highly concentrated dispersions and in opaque systems.[25] Ultrasound techniques have previously been used to study dense solid–liquid flows within fluidized beds.[26,27] Specifically, particle volume fractions ranging from 0.27 to 0.70 and particle size distributions between 500 and 1250 μm were measured. Ultrasound techniques have been applied to porosity and compressibility measurements in liquid suspended particles,[28] determining particle size distribution (PSD) as demonstrated by Wöckel et al.[29] and Nguyen et al.,[30] as well as for evaluating particle and bubble velocity profiles and porosity in porous materials as shown by Zhou et al.[31] Other research areas that can potentially benefit from fast and noninvasive measurements enabled by ultrasound techniques, include drop coalescence,[32,33] thinning and rupture of liquid sheets,[34] and contact line motion.[35] The speed of ultrasound in a liquid can vary depending on the liquid type and temperature. In two-phase systems of immiscible liquids or of a solid and a liquid phase, the mixture volume fraction can be calculated from the speed of sound in each phase and in the two-phase mixture. From measurements of the ultrasound attenuation through a dispersion, the size distributions of the dispersed phase can be calculated.[26] Ultrasound speed measurements have been employed to calculate drop size distributions ranging from 0.25 to 2 mm and low dispersed phase volume fractions ranging from 0.0053 to 0.042 in liquid–liquid dispersions formed in a stirred vessel.[24]

However, challenges may arise in signal post-processing, especially when the sound waves interact with multiple interfaces in multiphase mixtures. Furthermore, the sensitivity of sound waves to temperature and humidity can complicate technique development in environments where these factors are uncontrolled. Notwithstanding these challenges, ultrasound techniques can swiftly characterize various flow features, making them particularly valuable for online measurements and process control applications.

In this study, we applied ultrasound techniques for the first time to the characterization of dispersions formed in confined impinging jets in small channels. We developed signal post-processing methodologies to obtain from sound speed and attenuation measurements the volume fraction and the drop size distribution in a test channel of 2 mm inner diameter. To validate the ultrasound findings, a high-speed imaging method was employed to capture time-resolved images of the drops at the same time and location as the ultrasound transducers. In Secs. I–V, Sec. II elaborates on the experimental methodology, Sec. III describes the data post-processing for both ultrasound and imaging techniques, Sec. IV discusses the results, and Sec. V summarizes the conclusions.

II. EXPERIMENTAL SETUP AND METHODOLOGY
A. Experimental setup

Dispersions of kerosene oil and glycerol/water were generated in confined impinging jets (CIJ). One of the two phases is expected to be dispersed by the impact with the other phase depending on operating conditions. The two liquid phases have different refractive indexes so they can be imaged, and their properties can be found in Table I. The experimental setup of the CIJ is shown in Fig. 1(a). The impinging jets have an inner diameter of 0.5 mm and consist of two channels drilled perpendicular to each other, in the central plane of an acrylic block with dimensions $51 \times 25 \times 75$ mm^3. The formed mixture enters two opposite transparent FEP tubes, each with 2 mm inner diameter. The two fluids are introduced to the jets via two Ecom pumps (ECP2300).

B. Setup for high-speed imaging

The setup for the high-speed imaging experiments can be seen in Fig. 1(a). Imaging was carried out in one of the FEP tubings, 15 cm downstream of the impinging jets outlet. At the measurement point the tubing was enclosed within a visualization box filled with a 0.10 glycerol/water mixture that has a refractive index (1.344) close to that of the FEP tubing (refractive index of 1.346) to reduce the optical distortions caused by the curved tubing wall, and improve the quality of the high-speed images; for the ultrasound measurements a box is not required. The test section was back illuminated with an LED light. Images were captured with a high-speed camera (Phantom V1212) that had a ×12 monozoom lens (Navitar) and a ×2 add-on lens, at 3000 fps. The camera has 640×480 pixels giving a spatial resolution of the images equal to 4.64 μm/pixel. The lens was chosen for its good edge flatness and clarity. Images were processed using an in-house code developed with MIPAR, a commercial software developed within MATLAB's matrix processing algorithms and a recipe-based work flow.[36] For each case, 300 images were processed with an error of ± 4.64 μm on estimating the droplet diameter.

In impinging jets, the dispersed phase size distribution is related to the properties of both phases, the design of the jets, and the flow rate of the two phases. To investigate this, we carried out experiments for two different cases, namely cases 1 and 2. In case 1, kerosene oil was the dispersed phase, while in case 2, the aqueous phase (glycerol/water mixture) was the dispersed phase. For each case, we measured both the volume fractions and the drop size distributions under various experimental conditions using both ultrasound and high-speed imaging techniques. For the volume fraction studies, total flow rates of 60 ml/s were used for three volume fractions of the dispersed phase, namely 0.02, 0.05, and 0.10. The same conditions were used for the drop size distribution measurements with ultrasound. However, drop

TABLE I. Physical properties of the test fluids at room temperature and normal pressure.

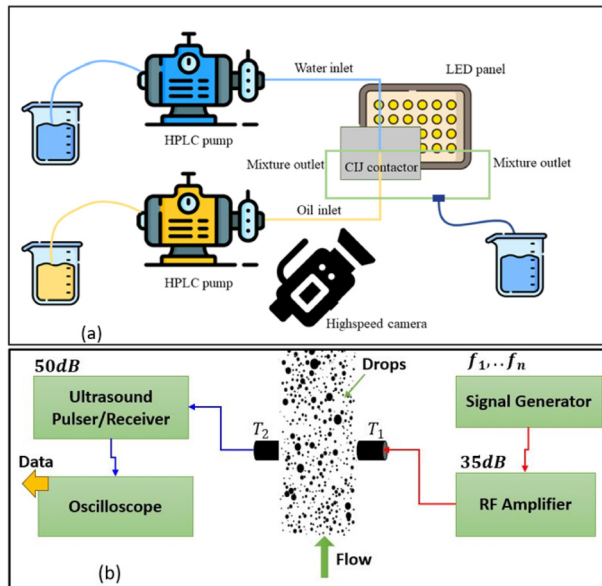| Properties	Kerosene oil	Water/glycerol
Density (kg/m^3)	795	1027
Viscosity (kg/m s)	0.002 04	0.001 38
Sound speed (m/s)	1329	1498
Refractive index	1.44	1.34

FIG. 1. (a) A schematic depiction of the CIJ experimental setup with high-speed camera and (b) the ultrasound circuit diagram, T_1 transmitting transducer, and T_2 receiving transducer.
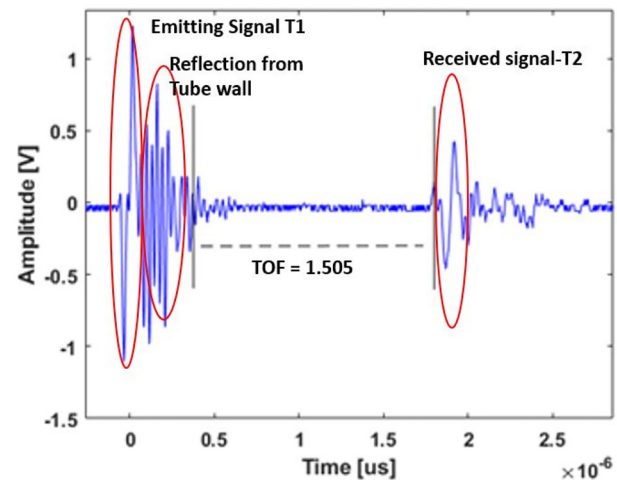

FIG. 2. Ultrasound wave propagation through the 2 mm tube in confined impinging jets. It displays the ultrasound wave released by transducer T_1, which is partly reflected by the tube wall. The signal then travels through the kerosene oil within the tube and is detected by transducer T_2.

sizes from imaging were only obtained at 0.02 and 0.05 dispersed phase volume fractions for both cases 1 and 2. This is because it is challenging to obtain drop sizes from imaging at high fractions of the dispersed phase because of multiple reflections and overlapping of neighboring droplets.

C. Setup for ultrasound measurements

A schematic diagram of the ultrasound equipment setup is shown in Fig. 1(b). The ultrasound transducers, which are 3/4″ in diameter, were positioned just after the visualization box. To measure drop sizes, two transducers were used: one as a transmitter and the other as a receiver. Both transducers were the RTD2250, which has a diameter of 3/4″ resonating 20 MHz, within a range of 1–40 MHz. Additionally, for measuring the drop volume fraction, two more transducers were employed, serving as both the receiver and emitter. These were the RTD2550, also 3/4″ in diameter, resonating at 2 MHz, with a frequency range of 1–5 MHz. These transducers were both manufactured by Sonatest. The ultrasound signal was generated using a function generator (33500B, Keysight), then amplified by 35 dB using an RF amplifier (TS500-C, Accel Instruments). This signal was transmitted through the test section via transducer T_1. Ultrasound gel is used between the transducers and the tube wall to eliminate any trapped air and reduce sound wave reflections from the wall. The ultrasound signal was then propagated through the dispersion, received by transducer T_2, and collected via the ultrasound pulser/receiver [see Fig. 1(b)], where it was amplified up to 50 dB. Finally, the digitized signal was captured by an oscilloscope (Keysight-DSOX3014T) and transferred to a computer for further signal post-processing.

Figure 2 illustrates the propagation of the ultrasound signal through the tube filled with kerosene oil. It depicts the emission of the signal from transducer T_1 (first pulse), its reflection from the tube wall

(second pulse, with multiple reflections visible due to the ultrasound gel application between the transducer and the tube wall and the inner and outer tube walls), and the transmission of the signal through the oil to the opposite side of the wall where it is received by transducer T_2 (last pulse, with multiple reflections, similar to those of transducer T_1). The time of flight (TOF) (the time that the sound wave takes to propagate through the tube inner diameter (2 mm) from T_1 to T_2 was found to be equal to 1.505×10^{-6} s for kerosene oil and 1.335×10^{-6} s for glycerol/water.

We employed two different measurement techniques, namely ultrasound propagation speed for calculating the dispersed phase volume fraction and ultrasound attenuation coefficient for calculating the drop size distribution. The ultrasound wave propagation speed depends on the physical properties of the two phases as well as their volume fraction in the dispersion and can be calculated using the following equation:

$$C = \frac{D}{t},\qquad(1)$$

where C denotes the sound speed, t denotes the time for the sound wave to travel within the fluid, and D is the tube inner diameter. As the ultrasound travels through the dispersion, various interactions occur between the ultrasound waves and the phases, leading to the attenuation (reduction in amplitude) of the ultrasound wave. These interactions encompass viscous dissipation (i.e., the oscillation of drops due to the density contrast between the drop and the continuous phases), absorption due to factors such as the viscosity and temperature of the liquid, as well as the frequency of the sound waves, reflections when sound waves encounter an interface, which depends on the acoustic impedance of the two phases, and scattering losses when the size of the drop is of the order of the ultrasound wavelength. In liquid–liquid dispersions, scattering primarily contributes to attenuation. The attenuation coefficient, α, of an ultrasound wave emitted at frequency f

and propagated through a dispersion over the tube diameter D can be calculated using the following equation:

$$\alpha = -\frac{1}{D} ln\left(\frac{A_o}{A_1}\right), \tag{2}$$

where A_o is the amplitude of the attenuated signal (the signal transmitted through the dispersion) and A_1 is the amplitude of the reference signal (the signal transmitted through the continuous phase only).

III. DATA POST-PROCESSING

A. Ultrasound

1. Volume fraction measurements

Two models have been proposed by Urick[37] and Atkinson and Wells,[38] to derive the dispersed phase volume fraction from ultrasound speed measurements. Both models operate under the assumption that the scattering effects are insignificant when the wavelength of the emitted sound wave greatly exceeds the characteristic size of the dispersed phase. Specifically, the sound wave was emitted at a frequency of 2 MHz, ensuring that the wavelength ($750\,\mu m$) was larger than the expected drop sizes. To obtain the drop volume fraction, the following steps were followed: (a) The TOF in the tube filled with oil was measured and from this, the sound speed in kerosene oil, C_k, was found to be equal to 1329 m/s. (b) The TOF in the tube filled with the glycerol/water mixture was measured and from this the sound speed, C_g, was found to be equal to 1498 m/s. (c) The sound speed was measured at the different oil aqueous phase dispersions, C_s, in the tube. (d) From the three measured sound speeds, the dispersed phase volume fractions under different conditions are calculated as follows:[26]

$$\varphi = \frac{-B \pm \sqrt{B^2 - 4AD}}{2A}, \tag{3}$$

where,　　　　$A = (C1 - rC2)(1 - r),$

$$B = 2rC_2 - C_1 + r^2C_2 + 2r(1 - C_1 - r),$$
$$D = r(1 + 2r)(1 - C_2),$$
$$r = \rho_k/\rho_g, \quad C_1 = \frac{C_s^2}{C_k^2}, \quad C_2 = \frac{C_s^2}{C_g^2},$$

where ρ_k and ρ_g are the densities of kerosene oil and glycerol/water, respectively.

2. Drop size distribution measurements

The attenuation of ultrasound in a dispersion is influenced by the thermophysical characteristics of the component phases, the drop size, the drop volume fraction, and the emitted ultrasound wave frequency. Mainly, the thermophysical properties encompass the density, thermal expansion coefficient, heat capacity, thermal conductivity, and viscosity of both phases.[39–41] Regarding dispersions, scattering becomes a primary cause of attenuation, linked to the drop size and density.[42,43] Moreover, multiple scattering occurs in the presence of many drops.

The theoretical ultrasound attenuation coefficient α_k is related to the extinction coefficient K, the emitted frequency of the sound wave f, and the size of the dispersed phase r, via the Lambert–Beer law[44] as follows:

$$\alpha_k = \int_{r_{min}}^{r_{max}} K(f_i, r)q(r)dr, \tag{4}$$

where r_{min} and r_{max} are the lower and upper limits of the drop size ranges, α_k is the attenuation coefficient that is found experimentally from Eq. (2), $q(r)$ is the drop number frequency distribution, and K is given by[44]

$$K = \frac{4}{9}S^4 + \left(\frac{\rho_k}{\rho_g} - 1\right)^2 \times \left(\frac{48\sigma^2(1 + \sigma)S}{81(1 + \sigma)^2 + 16\sigma^4\left(\frac{\rho_d}{\rho_c} + \frac{1}{2} + \frac{9}{4\sigma}\right)^2}\right), \tag{5}$$

$$\sigma = \sqrt{\frac{\pi\rho_d f r^2}{4\mu_d}}, \tag{6}$$

$$S = \frac{\pi r}{\lambda}, \tag{7}$$

where μ_d is the viscosity of the dispersed phase, f is the emitted frequency, ρ_d is the density of the dispersed phase, ρ_c is the density of the continuous phase, and λ is the wavelength of the emitted wave. Equation (4) is the Fredholm integral and can be approximated by its discretized version[45] as follows:

$$\alpha_k = \varphi \sum_j K(f_i, r_j)q_j\Delta(r_j). \tag{8}$$

For discrete drop size intervals, j, and different measuring frequencies, i, the above becomes a set of linear equations,

$$G = KF, \tag{9}$$

where F is the vector of the drop size distribution, $F = \varphi\,q(r_j)\Delta(r_j)$, and K is the matrix of the extinction coefficient calculated from Eq. (5), $G = \alpha_k$ is the attenuation coefficient spectra, obtained experimentally from Eq. (2). The drop size distribution can be calculated from the inverse of Eq. (9) as

$$F = G \times K^{-1}. \tag{10}$$

The solution of Eq. (10) tends to be unstable and to overcome this, Eq. (11) is solved instead,

$$F = \left(K^T K + \gamma(K^{-1})^T K^{-1}\right)^{-1} K^T G. \tag{11}$$

Here, γ is the Lagrange multiplier which gives a relative weight to K^{-1}, and the solution of F represents the drop size distribution. In the matrix representation of Eq. (11), the value of γ is chosen to yield minimum error, as calculated by $\sum E^2 = (KF - G)^T(KF - G)$. The usual procedure for applying this equation is to choose several values for γ in equation $F = \left(K^T K + \gamma(K^{-1})^T K^{-1}\right)^{-1} K^T G$, then calculate F and by using the F values estimate the error in $\sum E^2 = (KF - G)^T(KF - G)$. The value of gamma which gives the least error $\sum E^2$ is finally chosen. To determine the drop size distribution using ultrasound attenuation coefficient spectra, the following steps are taken: (a) ultrasound waves with excitation frequencies ranging from 5 to 18 MHz are sent through the continuous phase only, and the signal amplitudes for each frequency are measured; (b) signals with the same frequencies and
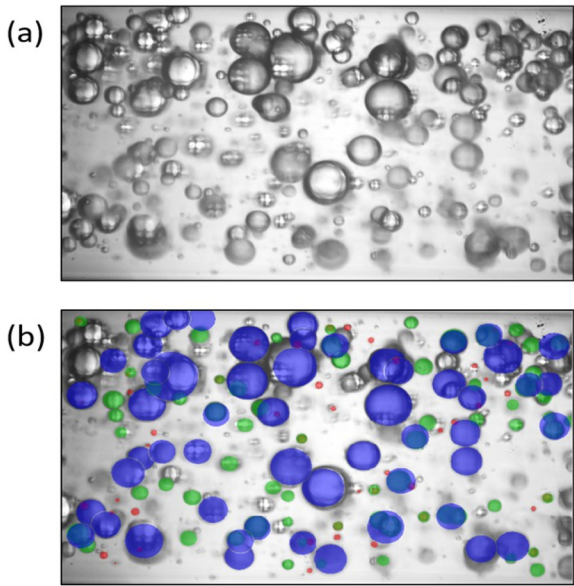
FIG. 3. Schematic of image processing. (a) Raw image from high-speed imaging. (b) Processed image with the drop size brackets used in the Hough transform indicated with different colors.

intensities are then propagated through a dispersion, and their signal amplitudes are measured; (c) the attenuation coefficients are calculated using Eq. (2); (d) the ultrasound extinction coefficient is calculated using Eq. (5); (e) the mathematical model that relates the attenuation coefficient, frequency, volume fraction, and physical properties with the drop size distribution [Eq. (4)] is then needed. For that, a distribution of the drop sizes [e.g., generalized extreme value (GEV) distribution][47] is assumed [see Eq. (12)] in Eq. (4); and (f) the drop size distribution is calculated from the measured attenuation coefficient, calculated extinction coefficient, and the measured volume fraction using Eq. (11).

$$f(x; \mu, \sigma, \xi) = \frac{1}{\sigma} \exp\left[1 + \xi\left(\frac{x-\mu}{\sigma}\right)\right]^{-\frac{1}{\xi}} \left[1 + \xi\frac{x-\mu}{\sigma}\right]^{-1-\frac{1}{\xi}}, \quad (12)$$

where x is the variable, μ is the location parameter, σ is the scale parameter, and ξ is the shape parameter.

B. High-speed imaging

1. Drop size distribution measurements

The identification of drops in the images is based on the algorithm developed in MIPAR. To avoid counting the same drops, one image was selected for every 20 recorded images. An adaptive threshold was then applied to compare the grayscale value of each pixel in the image against the average of 30 neighboring values. Dark pixels were selected as initial estimation of drop edges. Appropriate dilation and erosion operations were applied to each group of 300 images to adapt the strength of illumination, while the Hough transform was used to search for circles with dark outlines. For example, for images of kerosene oil dispersed in the aqueous phase [Fig. 3(a)], three brackets of the Hough transform were included to cover the necessary range of drop sizes, which are marked in Fig. 3(b) with different colors. When the aqueous phase was dispersed in kerosene oil, where larger drops were present, up to seven brackets were used in the Hough transform to include all possible diameters.

IV. RESULT AND DISCUSSION

A. Drop volume fraction measurements

To obtain the drop volume fraction, the speed of sound was measured at an overall mixture flow rate of 60 ml/s, and input volume fractions of 0.02, 0.05, and 0.10 and the results can be seen in Table II. The experimental measurements were repeated three times, and standard deviations smaller than 0.135% were found.

The dispersed phase volume fractions were calculated using Eq. (3) and are also shown in Table II. As can be seen, the sound speed decreases with increasing dispersed input oil volume fraction. This is because the sound speed in oil is less than in the glycerol/water phase. The opposite happens when the dispersed glycerol/water input volume fraction increases.

In Figs. 4 and 5, the measured *in situ* volume fractions are compared against the input ones for cases 1 (oil dispersed) and 2 (aqueous phase dispersed), respectively. The close agreement between measured and input volume fractions up to 0.10 suggests that there is very little slip between the two phases and that the dispersion resembles that of well-mixed homogeneous flow.[46]

B. Drop size distribution measurements

To measure the drop size distribution using ultrasound, the ultrasound wave amplitudes were recorded separately for the two single phases, for excitation frequencies ranging from 5 to 18 MHz at intervals of 1 MHz (see Fig. 6, blue color for pure oil phase and pink color for pure aqueous phase).

Figure 6 shows that the ultrasound signal amplitude decreases with increasing emitted frequency. As the emitted frequency increases, the fluids absorb more energy from the sound waves, resulting in a decrease in the amplitude. The amount of sound attenuation in each fluid would depend on various factors, such as the density of the two phases, as well as the frequency of the sound wave. In general, sound

TABLE II. Sound speed at different dispersed phase volume fractions with either the kerosene oil or the glycerol/water as the dispersed phase at the overall flow rate of 60 ml/s.

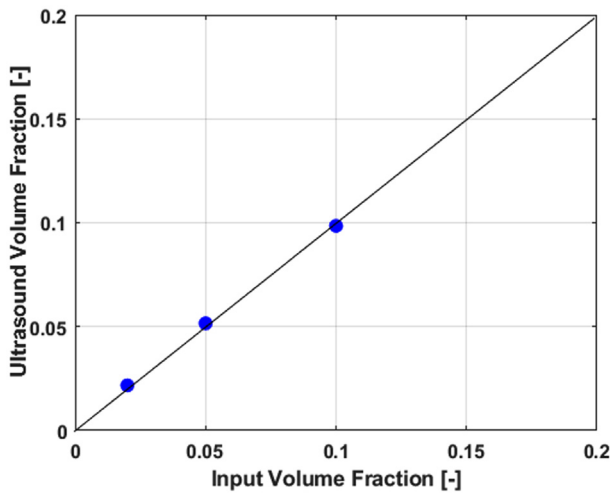| Flow rates ml/min		Sound speed m/s		Volume fraction	
Input dispersed	Input continuous	Oil dispersed	Water/glycerol dispersed	Oil dispersed	Water/glycerol dispersed
1.2	58.8	1492	1332	0.021	0.019
3	57	1484	1337	0.051	0.049
6	54	1472	1347	0.099	0.105

FIG. 4. Measured dispersed kerosene oil volume fraction by the ultrasound technique against input oil volume fraction.

FIG. 6. Amplitudes of the reference signal spectrum for various excitation signal frequencies measured in glycerol/water (pink color) and in kerosene oil (blue color).

waves are less attenuated in kerosene oil compared to glycerol/water due to the lower density of the oil.

The amplitudes were then measured during dispersed flows for the same frequencies, and the attenuation coefficients were calculated from Eq. (2) and are shown in Fig. 7.

Subsequently, an inversion method was applied to compute the droplet size distribution from the measured ultrasound attenuation coefficients (see Sec. III).

The frequency of the emitted ultrasound waves is related to the minimum and maximum drop sizes that can be detected. Higher frequencies generally result in better resolution and the ability to detect smaller drops. This is because high-frequency ultrasound waves have shorter wavelengths, allowing them to interact with and detect small drops more effectively. However, high-frequency waves also experience
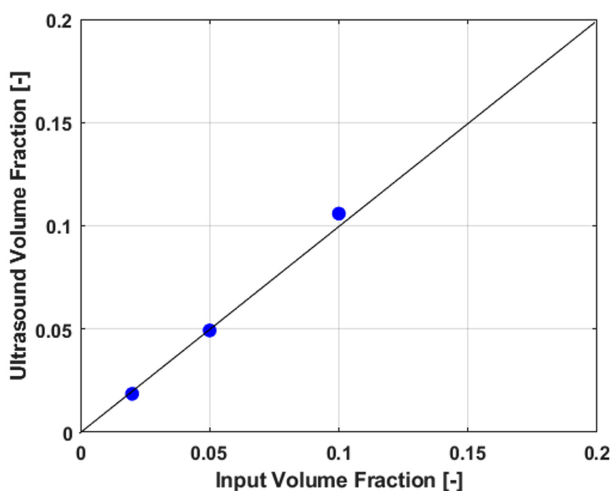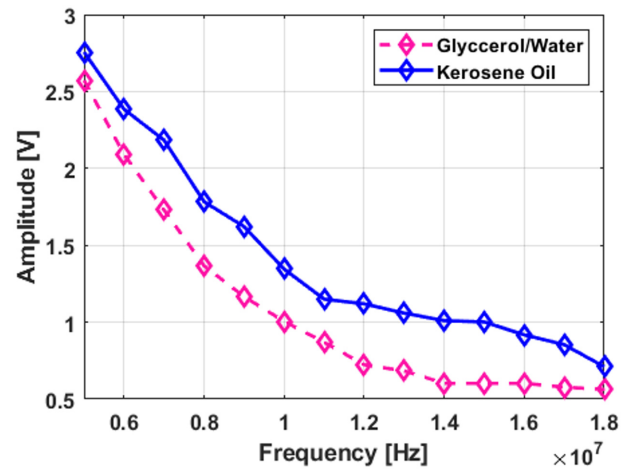
large attenuation and low penetration depth. Thus, for the selection of the ultrasound frequency, both resolution and penetration depth should be considered. Additionally, the inversion algorithm used in processing the attenuation data plays a significant role in determining the minimum drop size. Advanced inversion algorithms enhance resolution and measurement accuracy by improving data processing and interpretation, which can aid the measurement of small drops.

The drop size distributions obtained from both the ultrasound and imaging techniques are presented in Fig. 8 for case 1 and in Fig. 9 for case 2. Our ultrasound experimental configuration successfully detected drops as small as 32 μm, as shown in Fig. 8. The highest frequency used of 18 MHz corresponded to a short wavelength of 73 μm. This shorter wavelength inherently improves the resolution of ultrasound measurements, allowing for the detection of drops as small as 32 μm. The smallest drop size measured from high-speed imaging was

FIG. 5. Measured dispersed glycerol/water volume fraction by the ultrasound against input glycerol/water volume fraction.
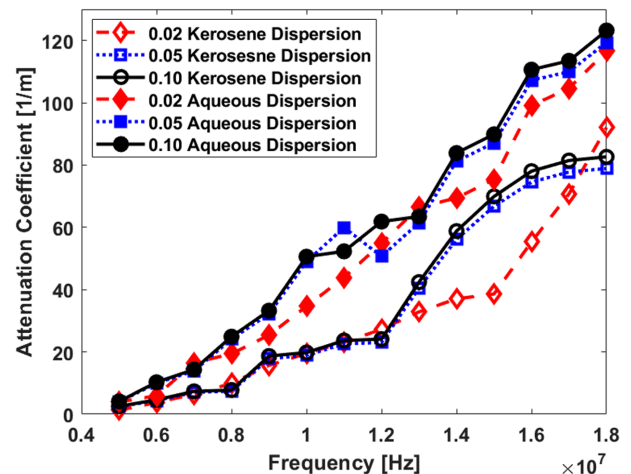

FIG. 7. Ultrasound attenuation coefficient spectra at different excitation frequencies.
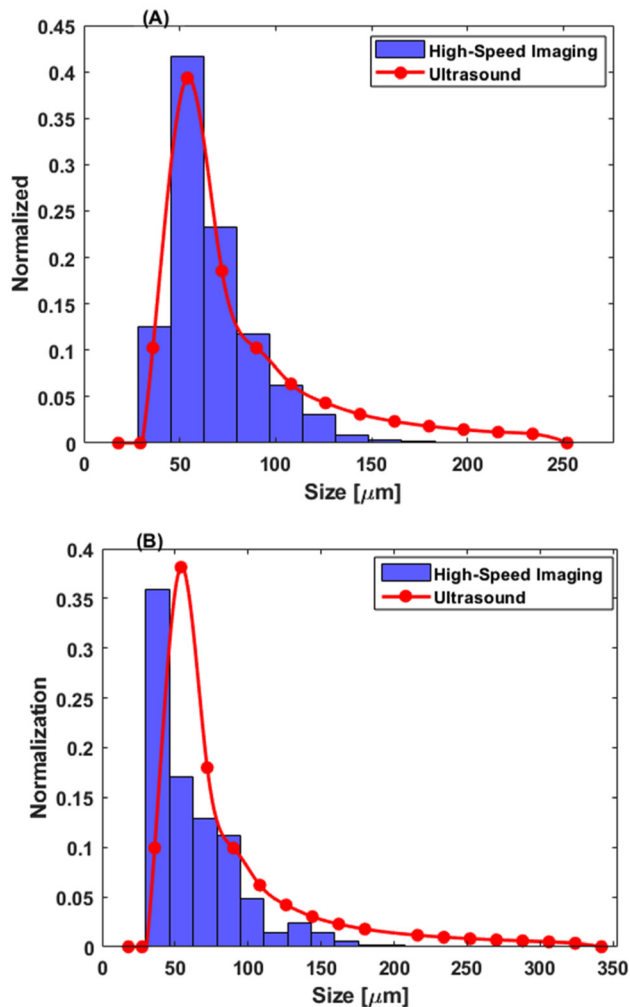
FIG. 8. Drop size distribution of oil drops in glycerol/water continuous phase (case 1) from the measured ultrasound attenuation coefficient spectra (red points) and imaging (blue bars). Dispersed phase fraction: (a) 0.02 and (b) 0.05.

about $16\,\mu$m. To compare the two techniques, only drop sizes above $32\,\mu$m were used from the imaging data.

As can be seen in Figs. 8(a) and 8(b) for glycerol/water continuous dispersions, the drop sizes measured with both techniques shifted to larger sizes as the dispersed phase fraction increased from 0.02 to 0.05. In addition, the imaging technique captured a higher percentage of smaller drops compared to the ultrasound technique, which gave a higher percentage of larger drops. This discrepancy can be attributed to the limitations of our current function generator, which restricts the emission of high ultrasound frequencies. However, this limitation could be addressed by utilizing instruments that allow high-frequency ultrasound waves (frequencies $> 18\,$MHz). Both techniques gave similar maximum drop sizes. For the 0.02 oil dispersion [Fig. 8(a)], the ultrasound technique measured drop sizes up to $240\,\mu$m, while imaging provided drop sizes up to $229\,\mu$m; for the case of 0.05 oil dispersion [Fig. 8(b)], ultrasound measured drop sizes up to $325\,\mu$m, while imaging gave drop sizes up to $321\,\mu$m.

Similarly, for aqueous dispersions (Fig. 9), imaging gave a higher percentage of smaller drops compared to ultrasound. For the 0.02 volume fraction [Fig. 9(a)], ultrasound measured drops up to $374\,\mu$m, whereas imaging measured drops up to $380\,\mu$m. For the 0.05 oil continuous dispersions [Fig. 9(b)], the largest drop sizes found were $695\,\mu$m from the ultrasound and $700\,\mu$m from imaging.

Based on the findings, it appears that while both ultrasound and imaging techniques yield similar measurements in terms of drop size ranges, there seems to be a discrepancy in the distribution of drops, with imaging showing a higher percentage of smaller drop sizes compared to ultrasound. This could potentially be attributed to assumptions during data processing for the two techniques. Moving forward, enhancing the measurement accuracy by expanding the frequency range in the ultrasound experiments could help address these differences.
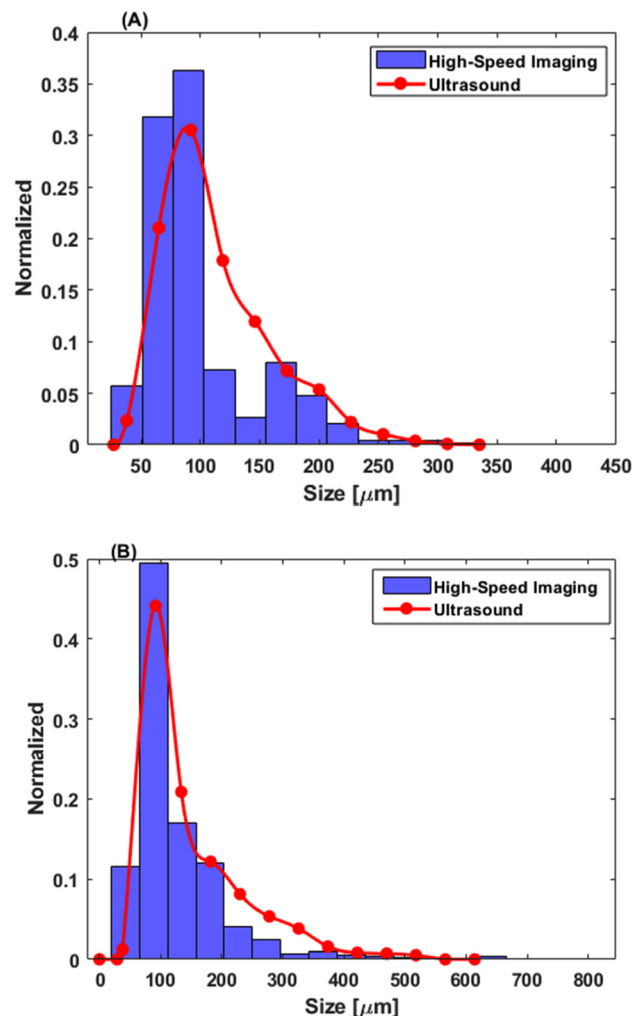

FIG. 9. Drop size distribution of aqueous drop in oil continuous phase (case 2) from the measured ultrasound attenuation coefficient spectra (red points) and imaging (blue bars). Dispersed phase fraction: (a) 0.02 and (b) 0.05.
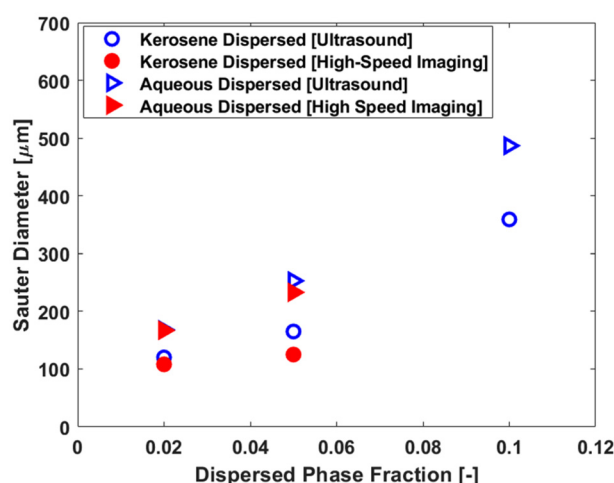
FIG. 10. Sauter mean diameters for all cases studied. Solid: high-speed imaging results; hollow: ultrasound results.

To quantitatively measure the interfacial area available in dispersions, the Sauter mean drop diameter (d_{32}) is often used as the representative drop diameter, which is defined as follows:

$$d_{32} = \frac{\sum_{i=1}^{n} \left(d_i^3 \right)}{\sum_{i=1}^{n} \left(d_i^2 \right)}. \tag{13}$$

In Fig. 10, the Sauter mean diameters are plotted against the dispersed phase volume fractions for all cases examined. The results from both techniques demonstrate strong agreement at dispersed phase fractions of 0.02, and 0.05 for both oil and aqueous continuous dispersions. In agreement with the distributions discussed before, at a dispersed phase fraction of 0.05, imaging shows smaller average drop sizes than ultrasound.

The trends suggest that as the dispersed phase fraction increases, the Sauter mean diameter also increases for both oil and aqueous phases dispersed. This could imply that at higher concentrations, droplets are more likely to coalesce into larger droplets or that the corresponding flow conditions at the impingement area of the jets favor the formation of larger droplets. Moreover, ultrasound measurements are capable of measuring at larger volume fractions compared to imaging, extending the measurements to dispersed phase fraction of 0.10. This is useful in systems where optical methods are challenged by multiple refractions/reflections or crowding, which occur at high dispersed phase fractions.

V. CONCLUSIONS

We applied ultrasound techniques to liquid–liquid dispersions formed by confined impinging jets in small channels (with 2 mm internal diameter) to measure for the first time the phase volume fractions and the drop size distributions. The drop volume fractions were obtained by measuring the speed of sound in the dispersions, while the drop size distributions were obtained from the inversion of the ultrasound wave attenuation coefficient spectra. We further compared the results on drop size distribution with data obtained from high-speed imaging of the dispersions. Experiments were conducted in CIJ for both kerosene oil dispersed (case 1) and glycerol/water dispersed (case

2) systems. Our findings revealed that the speed of sound is directly proportional to the aqueous phase volume fraction and is inversely proportional to the kerosene oil volume fraction. This is because the sound speed in the aqueous phase (1498 m/s) is higher than in kerosene oil (1329 m/s). It was found that volume fractions of the dispersed phase measured with ultrasound were close to the input ones, indicating insignificant slip in the confined impinging jets. Additionally, the drop size distributions obtained from ultrasound and from imaging showed reasonable agreement. The findings show that ultrasound measurement techniques can provide a range of properties in liquid–liquid dispersed flows, even at high dispersed phase fractions, where imaging is limited.

AUTHOR DECLARATIONS
Conflict of Interest

The authors have no conflicts to disclose.

Author Contributions

Fria Hossein: Conceptualization (equal); Data curation (equal); Formal analysis (equal); Methodology (equal); Supervision (equal); Validation (equal); Writing – original draft (equal); Writing – review & editing (equal). **Cong Duan:** Data curation (equal); Methodology (equal); Writing – review & editing (equal). **Panagiota Angeli:** Conceptualization (equal); Formal analysis (equal); Investigation (equal); Methodology (equal); Supervision (equal); Validation (equal); Writing – review & editing (equal).

DATA AVAILABILITY

The data that support the findings of this study are available from the corresponding author upon reasonable request.

REFERENCES

[1]H. Wang, A. Mustaffar, A. N. Phan, V. Zivkovic, D. Reay, R. Law, and K. Boodhoo, "A review of process intensification applied to solids handling," Chem. Eng. Process. **118**, 78–107 (2017).

[2]A. Sattari, P. Hanafizadeh, and M. Hoorfar, "Multiphase flow in microfluidics: From droplets and bubbles to the encapsulated structures," Adv. Colloid Interface Sci. **282**, 102208 (2020).

[3]D. Tsaoulidis and P. Angeli, "Effect of channel size on mass transfer during liquid–liquid plug flow in small scale extractors," Chem. Eng. J. **262**, 785–793 (2015).

[4]P. Angeli and G. F. Hewitt, "Drop size distributions in horizontal oil-water dispersed flows," Chem. Eng. Sci. **55**, 3133–3143 (2000).

[5]J. Lovick and P. Angeli, "Droplet size and velocity profiles in liquid–liquid horizontal flows," Chem. Eng. Sci. **59**, 3105–3115 (2004).

[6]S. Hardt and G. Mchale, "Flow and drop transport along liquid-infused surfaces," Annu. Rev. Fluid Mech. **54**, 83–104 (2022).

[7]J. H. Xu, J. Tan, S. W. Li, and G. S. Luo, "Enhancement of mass transfer performance of liquid–liquid system by droplet flow in microchannels," Chem. Eng. J. **141**(1–3), 242–249 (2008).

30 August 2024 09:01:07

[8] A. N. Manzano Martínez, M. Assirelli, and J. van der Schaaf, "Droplet size and liquid-liquid mass transfer with reaction in a rotor-stator Spinning Disk Reactor," Chem. Eng. Sci. **242**, 116706 (2021).

[9] J. Lovick, A. A. Mouza, S. V. Paras, G. J. Lye, and P. Angeli, "Drop size distribution in highly concentrated liquid–liquid dispersions using a light back scattering method," J. Chem. Technol. Biotechnol. **80**, 545–552 (2005).

[10] S.-J. Wang, Z.-H. Shi, T.-L. Yao, W.-F. Li, and Q.-G. Lin, "Experimental and numerical study of liquid film by jet impingement: Based on contact angle model," Phys. Fluids **35**, 085104 (2023).

[11] D. Tsaoulidis and P. Angeli, "Liquid-liquid dispersions in intensified impinging-jets cells," Chem. Eng. Sci. **171**, 149–159 (2017).

[12] U. Hampel, J. Otahal, S. Boden, M. Beyer, E. Schleicher, W. Zimmermann, and M. Jicha, "Miniature conductivity wire-mesh sensor for gas-liquid two phase flow measurement," Flow Meas. Instrum. **20**, 15–21 (2009).

[13] R. Dai, N. Jin, Q. Hao, W. Ren, and L. Zhai, "Measurement of water holdup in vertical upward oil–water two-phase flow pipes using a helical capacitance sensor," Sensors **22**, 690 (2022).

[14] A. Abdollahi, R. N. Sharma, and A. Vatani, "Fluid flow and heat transfer of liquid-liquid two phase flow in microchannels: A review," Int. Commun. Heat Mass Transfer **84**, 66–74 (2017).

[15] S. T. Thoroddsen, T. G. Etoh, and K. Takehara, "High-speed imaging of drops and bubbles," Annu. Rev. Fluid Mech. **40**, 257–285 (2008).

[16] L. Zhai, X. Meng, Z. Meng, H. Zhang, and N. Jin, "Measurement and prediction of droplet entrainment in inclined liquid–liquid flow by PLIF method," IEEE Trans. Instrum. Meas. **72**, 4502913 (2023).

[17] A. Timgren, G. Trägårdh, and C. Trägårdh, "Application of the PIV technique to measurements around and inside a forming drop in a liquid–liquid system," Exp. Fluids **44**, 565–575 (2008).

[18] J. C. R. Reis, I. M. S. Lampreia, Â. F. Santos, M. L. C. J. Moita, and G. Douhéret, "Refractive index of liquid mixtures: Theory and experiment," ChemPhysChem **11**, 3722–3733 (2010).

[19] Q. Yang, N. Jin, F. Wang, and W. Ren, "Measurement of gas phase distribution using multifiber optical probes in a two-phase flow," IEEE Sens. J. **20**, 6642 (2020).

[20] J. Zhang and B. J. Balcom, "Magnetic resonance imaging of two-component liquid-liquid flow in a circular capillary tube," Phys. Rev. E **81**, 056318 (2010).

[21] R. R. Tromp and L. M. Cerioni, "Multiphase flow regime characterization and liquid flow measurement using low-field magnetic resonance imaging," Molecules **26**, 3349 (2021).

[22] N. M. Hasan and B. J. Azzopardi, "Imaging stratifying liquid–liquid flow by capacitance tomography," Flow Meas. Instrum. **18**, 241–246 (2007).

[23] H. Y. Wei and M. Soleimani, "Two-phase low conductivity flow imaging using magnetic induction tomography," Prog. Electromagn. Res. **131**, 99–115 (2012).

[24] F. Hossein, P. S. Farias, X. Qi, and P. Angeli, "Application of ultrasound techniques to liquid-liquid dispersed flows," Int. J. Multiphase Flow **169**, 104606 (2023).

[25] X. Liu, X. Yu, X. Yu, H. Zhou, S. Zhang, J. Li, and L. Yang, "Measurement of jet gas–liquid interface fluctuations based on ultrasonic scattering," Phys. Fluids **36**, 013333 (2024).

[26] F. Hossein, M. Materazzi, P. Lettieri, and P. Angeli, "Application of acoustic techniques to fluid-particle systems—A review," Chem. Eng. Res. Des. **176**, 180–193 (2021).

[27] F. Hossein, M. Materazzi, M. Errigo, P. Angeli, and P. Lettieri, "Application of ultrasound techniques in solid-liquid fluidized bed," Measurement **194**, 111017 (2022).

[28] E. Han, N. Van Ha, and H. M. Jaeger, "Measuring the porosity and compressibility of liquid-suspended porous particles using ultrasound," Soft Matter **13**, 3506–3513 (2017).

[29] S. Wöckel, U. Hempel, R. Weser, B. Wessely, and J. Auge, "Particle characterization in highly concentrated suspensions by ultrasound scattering method," Procedia Eng. **47**, 582–585 (2012).

[30] T. N. Tran, T. Shibata, T. Norisuye et al., "Determination of particle size distribution and elastic properties of silica microcapsules by ultrasound spectroscopy," Jpn. J. Appl. Phys. **55**, 07KC01 (2016).

[31] B. Zhou, K. H. Fraser, C. Poelma, J.-M. Mari, R. J. Eckersley, P. D. Wein, and M. X. Tang, "Ultrasound imaging velocimetry: Effect of beam sweeping on velocity estimation," Ultrasound in Medicine and Biology **39**, 1672–1681 (2013).

[32] J. D. Paulsen, R. Carmigniani, A. Kannan, J. C. burton, and S. R. Nagel, "Coalescence of bubbles and drops in an outer fluid," Nat. Commun. **5**, 3182 (2014).

[33] J. D. Paulsen, J. C. Burton, S. R. Nagel, S. Appathurai, M. T. Harris, and O. A. Basaran, "The inexorable resistance of inertia determines the initial regime of drop coalescence," Proc. Natl. Acad. Sci. U. S. A. **109**, 6857–6861 (2012).

[34] V. Garg, S. S. Thete, C. R. Anthony, and O. A. Basaran, "Local dynamics during thinning and rupture of liquid sheets of power-law fluids," J. Fluid Mech. **942**, A15 (2022).

[35] J. H. Snoeijer and B. Andreotti, "Moving contact lines: Scales, regimes, and dynamical transitions," Annu. Rev. Fluid Mech. **45**, 269–292 (2013).

[36] J. M. Sosa, D. E. Huber, B. Welk, and H. L. Fraser, "Development and application of MIPAR™: a novel software package for two- and three-dimensional microstructural characterization," Integr. Mater. Manuf. Innovation **3**, 123–140 (2014).

[37] P. Atkinson and P. N. T. Wells, "Pulse-doppler ultrasound and its clinical application," Yale J. Biol. Med. **50**, 367 (1977). See https://www.ncbi.nlm.nih.gov/pmc/articles/PMC2595531/.

[38] R. J. Urick, "A sound velocity method for determining the compressibility of finely divided substances," J. Appl. Phys. **18**, 983–987 (1947).

[39] Y. Tsujimoto, M. Morimoto, N. Nitta, and I. Akiyama, "Ultrasonic measurement of sound velocity fluctuations in biological tissue due to ultrasonic heating and estimation of thermo-physical properties," J. Med. Ultrason. **46**, 35–43 (2019).

[40] T. Tang, C. Shen, and L. Huang, "Propagation of acoustic waves and determined radiation effects on axisymmetric objects in heterogeneous medium with irregular interfaces," Phys. Fluids **36**, 012023 (2024).

[41] S. J. Patey and J. P. Corcoran, "Physics of ultrasound," Anaesth. Intensive Care Med. **22**, 58–63 (2021).

[42] F. Hossein and P. Angeli, "A review of acoustofluidic separation of bioparticles," Biophys. Rev. **15**, 2005 (2023).

[43] D. J. McClements and J. J. Coupland, "Theory of droplet size distribution measurements in emulsions using ultrasonic spectroscopy," Colloids Surfaces, A **117**, 161–170 (1996).

[44] M. Su, F. Xu, X. Cai, K. Ren, and J. Shen, "Optimization of regularization parameter of inversion in particle sizing using light extinction method," China Particuol. **5**, 295–299 (2007).

[45] U. Riebel and F. Löffler, "The fundamentals of particle size analysis by means of ultrasonic spectrometry," Part. Part. Syst. Charact. **6**, 135–143 (1989).

[46] J. Y.-L. Lum, T. Al-Wahaibi, and P. Angeli, "Upward and downward inclination oil-water flows," Int. J. Multiphase Flow **32**, 413–435 (2006).

[47] B. A. A. Abdulali, M. A. A. Bakar, K. Ibrahim, and N. M. Arif, "Extreme value distribution: An overview of estimation and simulation," J. Probab. Stat. **2022**, 5449751.